Korean J. Chem. Eng., **19**(4), 694-702 (2002)

Numerical Analysis of the Electro-discharge Machining Process for Alumina-Titanium Carbide Composite II. Unsteady State Approach

Young-Cheol Ahn† and Young-Seup Chung

Division of Chemical Engineering, Kyungnam University, Masan 631-701, Korea
(*Received 6 August 2001 • accepted 1 February 2002*)

Abstract–The electrical discharge machining process of a ceramic composite material consisting of alumina and titanium carbide has been modelled as an unsteady state mathematical model and solved by using Galerkin's implicit finite element method. For several selected currents and powers the spark melted and sublimated the workpiece to form a crater which gradually expanded outwards. The size and shape of the crater anticipated by the computation were in good agreement with the scanning electron micrograph of the crater formed in an experiment. An increased electric current and duty factor would increase the material removal rate in expense of roughened surface and deteriorated mechanical properties.

Key words: Electro-Discharge Machining, Alumina, Titanium Carbide, Unsteady State Analysis, Finite Element Method

INTRODUCTION

Traditional type of machining process for a ceramic composite material mainly consists of mechanical processes such as cutting and grinding. Recently, novel machining processes such as electro-discharge machining, supersonic machining, laser machining, and combinations of these processes were developed and have found their specific areas of application. In particular, electro-discharge machining (EDM) has many merits such as high speed, precision, and machinability of complex shape. The only limitation of EDM is that the workpiece should have an electrical conductivity, since the machining is induced by the heat emitted from an electrical spark between workpiece and electrode. Therefore, basically a ceramic material or ceramic matrix composite of low electrical conductivity cannot be machined with the EDM. However, if the nonconductive ceramics are mixed with a conductive material, then according to the percolation theory the composite can have a conductivity when the composition of electrically conductive material is over the critical value and thus can be machined with EDM.

Since EDM process has various merits as mentioned above, its usage has been widely exploited by machinists and its principles have become well understood by the efforts of many researchers during the past decades. Researches have been focused to identify the basic principles of EDM. Part of the researches approached the problem theoretically in order to identify the melting mechanism involved. For an exact analysis, one should have a thorough understanding of the related phenomena such as multiplicity of discharge, moving of boundary, convection and radiation of heat to dielectric liquids and surroundings, and melting of electrodes, etc. Dharmadhikari and Sharma [1980] assumed multiple heat sources in determining the material removal rate for a single pulse, while Snoeys and Van Dyck [1971] applied thermal conduction theory in establishing relationships between the depth of melting and the parameters such as discharge energy, discharge time, and property of electrode. For the process of machining a metal workpiece with disk-shaped heat source, Jilani and Pandey [1982, 1983] introduced vaporization of metal melts into their model in order to improve the accuracy of analysis. And, based on a stochastic model of the thermal process, Pandit and Rajurkar [1983] induced more realistic results for the material removal rate and heat-affected zone. These researches, however, could not precisely explain the electro-discharge machining process. There have been different kinds of approaches to the analysis of the EDM process, based on numerical simulation. One is finite element method and the other is finite difference method. Madhu et al. [1991] applied the former, while Gadalla and Cheng [1993] applied the latter. They introduced relatively specified mathematical models to their analysis and obtained more realistic results than the other analytical approaches described above. However, their models still have several unreasonable assumptions concerning energy of the source and properties of the material. Recently, in a finite element analysis by Ahn et al. [1997] for the EDM process, they introduced a more reasonable mathematical model and obtained somewhat interesting results for the special case of steady state approximation. In this research, based on the model developed by Ahn et al., a more realistic transient analysis has been performed by finite element method.

PROCESS MODELLING

1. Heat Transfer Model

Electricity is discharged between electrodes when a high voltage is applied across a short distance between them in a dielectric liquid. Electro-discharge machining, which makes use of this principle, is a sophisticated machining process that induces sparks between electrode and workpiece, and machines the workpiece with the heat developed as a result. There are two kinds of EDM processes: one is wire-cut EDM which is mainly used for making a mold with a

†To whom correspondence should be addressed.
E-mail: ycahn@kyungnam.ac.kr

wire electrode, and the other is die-sinking EDM which is used for cutting an arbitrarily shaped relief images with a pre-designed electrode. In this research, the analysis has been focused on the latter.

One cycle of the electro-discharge machining process starts with an induction period after the application of power. When a plasma is formed, the electricity is discharged during a very short time (~100 microseconds). Then, the power is disconnected and the process goes into a resting period. After the resting period, the power is on again and the process repeats the same cycle continuously. It is generally considered that there are a finite number of discharges per unit time and the location of discharge is varied every time. In order to analyze a complicated problem of this kind, it is necessary to simplify the model. Here, a spark of discharge is selected for analyzing the phenomena that occur during an electro-discharge machining process. In order to help understanding the situation, a schematic diagram of a typical spark is demonstrated in Fig. 1. When the electricity discharges as in the figure, the location that the spark strikes the workpiece and the amount of its energy are varied irregularly. Since an exact estimation of them is impossible, a cylindrical spark of uniform heat flux has been introduced as a model. Axisymmetrical distribution of heat has also been assumed in the cylindrical coordinate system. Therefore, changes of temperature in θ-direction can be neglected, that is, $\partial T/\partial\theta=0$, and the energy balance equation is written as follows.

$$\frac{\partial T}{\partial t}=\alpha\left[\frac{1}{r}\frac{\partial}{\partial r}\left(r\frac{\partial T}{\partial r}\right)+\frac{\partial^2 T}{\partial z^2}\right] \tag{1}$$

where α is thermal diffusivity expressed as $k/\rho C_p$. k is thermal conductivity, ρ is density, and C_p is specific heat of the material, respectively. The initial and boundary conditions for the domain of interest are summarized as follows.

(Initial Condition)

$$\text{At : } t=0 : T=T_0 \tag{2}$$

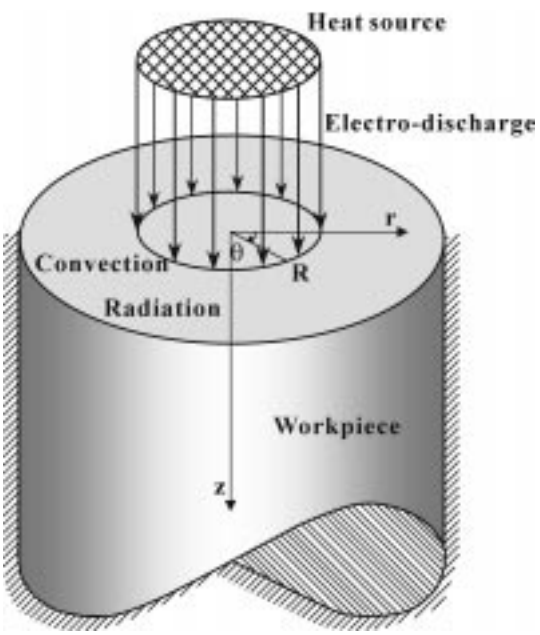

Fig. 1. Schematic diagram of a typical spark in an electro-discharge machining process.

(Boundary Conditions)

$$\text{At } r=\infty : \frac{\partial T}{\partial r}=0 ; \tag{3}$$

$$\text{At } z=\infty : \frac{\partial T}{\partial z}=0 ; \tag{4}$$

$$\text{At } r=0 : \frac{\partial T}{\partial r}=0 ; \tag{5}$$

$$\text{At } z=\delta(r,t),\ 0\le r\le R : -k\frac{\partial T}{\partial \underline{n}}=Q_a(r) ; \tag{6}$$

$$\text{At } z=\delta(r,t),\ R<r\le\infty : -k\frac{\partial T}{\partial \underline{n}}=h(T_f-T) ; \tag{7}$$

where T_0 is the initial temperature, $Q_a(r)$ is the heat flux of the spark in the direction normal to the boundary surface, h is the heat transfer coefficient, and T_f is the temperature of the dielectric liquid, respectively. Eqs. (3) and (4) denote the adiabatic condition at the boundary far from the spark, and Eq. (5) denotes the symmetry condition at the center axis. Eq. (6) denotes that at the boundary inside the region of electrical discharge the rate of conductive heat transfer equals the heat flux of the spark, while Eq. (7) denotes that at the boundary outside the region of electrical discharge the rate of conductive heat transfer equals the rate of convective heat transfer.

2. Finite Element Analysis

The above energy balance equation is transformed into a weak form by means of the variational method when Galerkin's finite element method is applied. That is,

$$0=\int_{\Omega^e}\left[v\frac{\partial T}{\partial t}+\alpha\frac{\partial v}{\partial r}\frac{\partial T}{\partial r}+\alpha\frac{\partial v}{\partial z}\frac{\partial T}{\partial z}\right]rdrdz-\oint_{\Gamma^e}vq_n ds \tag{8}$$

$$q_n=r\left(\alpha\frac{\partial T}{\partial r}n_r+\alpha\frac{\partial T}{\partial z}n_z\right) \tag{9}$$

where Ω^e denotes the domain of a finite element, and Γ^e denotes the face of the element. v is the bilinear shape function and q_n is

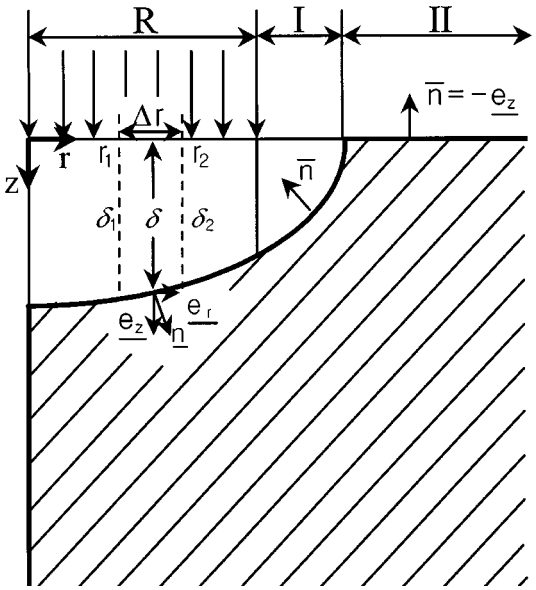

Fig. 2. Normal vector along the surface of the crater zone.

the gradient in the direction outward normal to the face of the element. n_r and n_z are the radial and the axial components of the outward normal vector to the face of the element, respectively.

The boundary surface near the spark is shown in Fig. 2 where the normal vector $\underline{n}$ to the boundary surface is expressed as

$$\underline{n} = \frac{(-\delta_r \underline{e}_r + \underline{e}_z)}{(1+\delta_r^2)^{1/2}} \tag{10}$$

Here, $\underline{e}_r$ and $\underline{e}_z$ are the unit vectors in the radial and the axial direction, respectively, δ is the depth of the crater, and δ_r is the radial derivative of δ expressed as

$$\delta_r = \frac{\partial \delta}{\partial r} = \frac{\delta_2 - \delta_1}{r_2 - r_1} \tag{11}$$

The normal vector $\bar{n}$ in the opposite direction to the normal vector $\underline{n}$ is obtained by

$$\bar{n} = -\underline{n} = \frac{(\delta_r \underline{e}_r - \underline{e}_z)}{(1+\delta_r^2)^{1/2}} = n_r \underline{e}_r + n_z \underline{e}_z \tag{12}$$

where n_r and n_z are expressed as

$$n_r = \frac{\delta_r}{(1+\delta_r^2)^{1/2}} \text{ and } n_z = -\frac{1}{(1+\delta_r^2)^{1/2}} \tag{13}$$

respectively. For the region inside the electrical discharge, according to the boundary condition, the gradient outward normal to the face of boundary elements is obtained by

$$q_n = -r\frac{Q_z n_z}{\rho C_p} \tag{14}$$

where Q_z, the axial component of the discharge heat flux Q, is the same as Q. For the region outside the electrical discharge, according to the boundary condition, the gradient outward normal to the face of boundary elements is obtained by

$$q_n = r\frac{h}{\rho C_p}(T_f - T) \tag{15}$$

where T_f is the bulk temperature of dielectric liquid, for which the room temperature is assigned outside the region of a crater (region II in Fig. 2) and the boiling point is assigned within the region of a crater (region I in Fig. 2).

Bilinear rectangular element was introduced in the region and the weak form of equations was applied to each element. The computational accuracy and effectiveness were compared for several meshes [Ahn et al., 1997], and finally the irregular mesh shown in Fig. 3 was chosen as the optimum mesh.

The dependent variable T can be approximated by interpolation between node values and is expressed in terms of bilinear interpolation functions as follows.

$$T(r,z,t) \approx \sum_{j=1}^{N} T_j^e(t)\psi_j^e(r,z) \tag{16}$$

where N is the number of nodes in an element, superscript e means an element and ψ_j^e means the j-th shape function. This equation is applied into Eq. (8) and, after some rearrangement, the following equation is obtained.

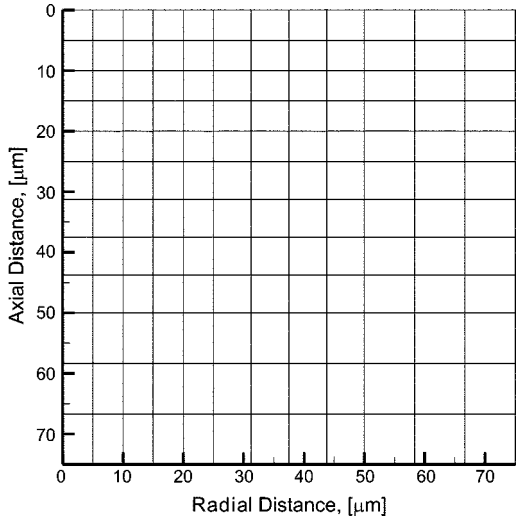

Fig. 3. Finite element mesh selected for the computation.

$$0 = \sum_{j=1}^{N}\left(M_{ij}^e \frac{dT_j^e}{dt} + K_{ij}^e T_j^e\right) - Q_i^e \tag{17}$$

where

$$M_{ij}^e = \int_{\Omega^e} \psi_i \psi_j r dr dz$$

$$K_{ij}^e = \int_{\Omega^e} \left(\alpha \frac{\partial \psi_i}{\partial r}\frac{\partial \psi_j}{\partial r} + \alpha \frac{\partial \psi_i}{\partial z}\frac{\partial \psi_j}{\partial z}\right) r dr dz$$

$$Q_i^e = \oint_{\Gamma^e} \psi_i q_n ds$$

This can be expressed in matrix form as

$$[M]\{\dot{T}\} + [K]\{T\} = \{Q\} \tag{18}$$

where $\dot{T}$ is the time derivative of the temperature.

In the approximation of the time term of the parabolic equation Galerkin's implicit method was introduced to give a stable solution as explained in the literature [Reddy, 1993]. The element equations derived were treated by the Newton-Raphson method and expanded to the entire region to give a banded matrix which is to be solved by the Gaussian elimination.

RESULTS AND DISCUSSION

The location of the spark is related to the surface roughness of electrode and workpiece, and its diameter is determined by the duty factor (DF) which is the ratio of the on-time to the sum of the induction time, on-time and off-time, and also by the discharge power. In this study, a spark of 50 μm diameter was assumed according to the literature [Dharmadhikari and Sharma, 1980; Madhu et al., 1991; Ahn et al., 1997]. The heat affected zone for each spark would be larger than the spark diameter, and therefore a cylindrical region three times as large as the spark diameter was introduced for analysis and the boundary conditions were assigned. The location of the boundary on which adiabatic conditions can be assumed should be far enough from the spark and is determined by calculating the thermal penetration depth [Bird et al., 1960] as follows.

$$\delta_D \doteq 4\sqrt{\alpha t} \tag{19}$$

Table 1. Physical properties of the ceramic composite workpiece

	Al_2O_3 (at 1,300 K)	TiC (at 1,800 K)	Al_2O_3 (66%) +TiC (33%)
ρ [kg/m^3]	3,975	4,890	4,237.2
C_p [cal/kg·K]	303.988	204.71	268.186
k [cal/m·s·K]	1.434	1.11	1.31
α [m^2/s]	1.187×10^{-6}	1.11×10^{-6}	1.153×10^{-6}
T_m [K]	2,315	3,489	2,679.27*

*Averaged value, but not actually assumed.

where δ_D is the thermal penetration depth, α is the thermal diffusivity, and t is the discharge time. For a discharge time of 130 μs, the thermal penetration depth would be ~50 μm. In this study, the distance from the center of the spark to the adiabatic boundary was assigned to be 75 μm that is three times as long as the spark radius and even longer than the penetration depth. Therefore, the boundary location is considered to be far enough from the center for the adiabatic condition to be applied.

The physical properties of the alumina-titanium carbide composite has been determined according to the mixing rule and the values thus obtained at the mid temperature between room and melting temperature are summarized in Table 1. However, the melting temperature of the ceramic composite does not follow the mixing rule, but preserves its components' own melting points.

The heat transfer coefficient should contain the effect of radiation in addition to the convection, and for the parametric range of the electrical discharge problem the correction factor by the radiation is known to be ~10% [Madhu et al., 1991; Bromley, 1950]. The heat transfer by radiation is computed by the following equation [Madhu, 1991].

$$h_r=\sigma\varepsilon(T^2+T_f^2)\,(T+T_f) \tag{20}$$

where σ is the Boltzmann's constant, ε is the emissivity, T_f is the temperature of the fluid. T is the surface temperature of the workpiece and assumed to be the average of the melting temperatures of alumina and titanium carbide. If the radial heat transfer coefficient h_r thus obtained is assumed to be 10% of the convective heat transfer coefficient, then the total heat transfer coefficient can be estimated to be 2345.67 cal/m^2·s·K.

The typical value of the discharge heat flux used for calculation corresponds to the electricity of 7 A and 51.3 V which is one of the several conditions tested in the electrical discharge machining experiment [Wang et al., 1997]. This is equivalent to the discharge flux of 2.812×10^{10} cal/m^2·s supplied through a circular area with radius of 25 μm. With the time increment (Δt) of 0.1 μs the temperature distribution inside the workpiece has been calculated and observed up to the discharge time of 130 μs. Fig. 4 shows the temperature distribution inside the workpiece at 10 μs after the start of discharge. It is seen that a hot spot is produced at the surface with a tempera-

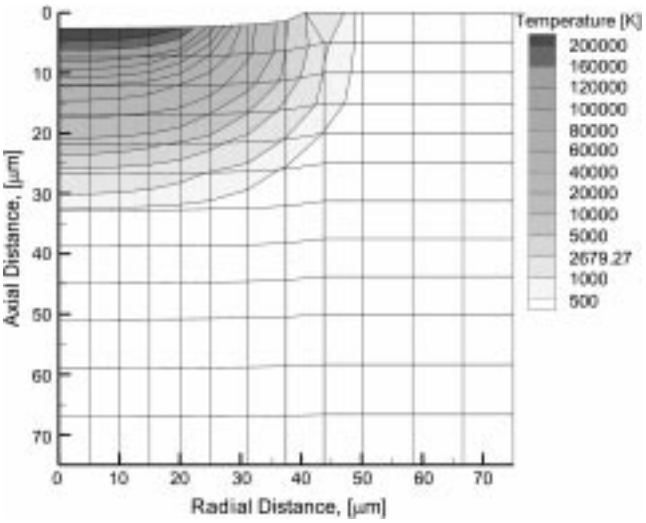

Fig. 5. Temperature distribution in the electro-discharge machined workpiece when 70 μs are elapsed after the onset of the on-time (current of 7 A and voltage of 51.3 V).

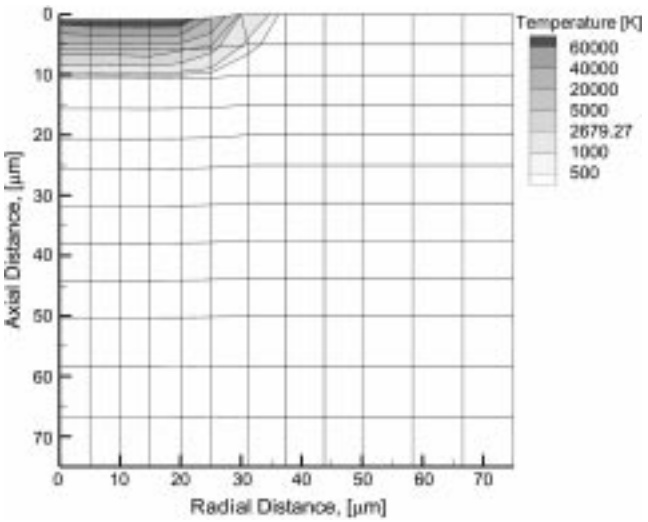

Fig. 4. Temperature distribution in the electro-discharge machined workpiece when 10 μs are elapsed after the onset of the on-time (current of 7 A and voltage of 51.3 V).

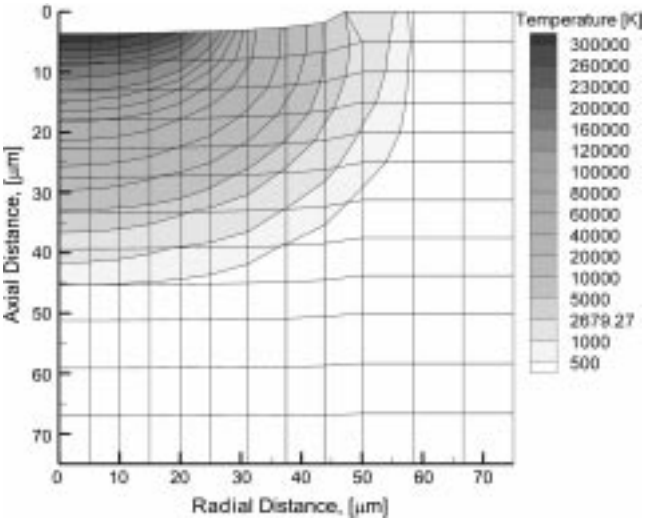

Fig. 6. Temperature distribution in the electro-discharge machined workpiece when 130 μs are elapsed after the onset of the on-time (current of 7 A and voltage of 51.3 V).

ture as high as 60,000 K at which melting and vaporization of the workpiece can occur. This means that the workpiece will start to melt and vaporize at the very early stage of discharge.

In Figs. 5 and 6 the temperature distributions at 70 μs and 130 μs are shown. As time passes, the highest temperature increases up to 200,000 K at 70 μs and to 300,000 K at 130 μs. And the contours move forward in the axial and radial direction. At the end of the discharge the contour of 500 K is located at 45 μm on the axial coordinate and at 60 μm on the radial coordinate. From this computational result, it can be said that the adiabatic boundary is adequately positioned as was verified by the penetration depth. If the melting temperature of the composite obtained by the mixing rule, 2679.27 K, is used for melting contour, it can be estimated that a crater of 35 μm depth and 45 μm radius will be formed. However, if the latent heat and redeposition of melted workpiece are taken into account, the actual temperature will be underestimated and the size of crater formed will become smaller than this estimation.

For the calculation of the depth of the crater being created after the onset of the spark, the location of the melting isotherm needs to be estimated exactly. The major factor that affects the speed of the moving melting isotherm is the latent heat of melting, and combining this with the specific heat will produce the correct location of the melting isotherm. The effects of the latent heat of evaporation and the recast of the once-melted workpiece were made to be incorporated by introducing the removal efficiency in calculating the actual thickness of the removed layer as follows:

$$d_c=\eta z_m \tag{21}$$

where η is the removal efficiency and z_m is the thickness of the melted layer. Madhu et al. [1991] defined the removal efficiency by the ratio of the removed volumes to the melted volume, but in this study it was defined by the ratio of the thickness of the removed layer to the thickness of the melted layer. The removal efficiency of 10%

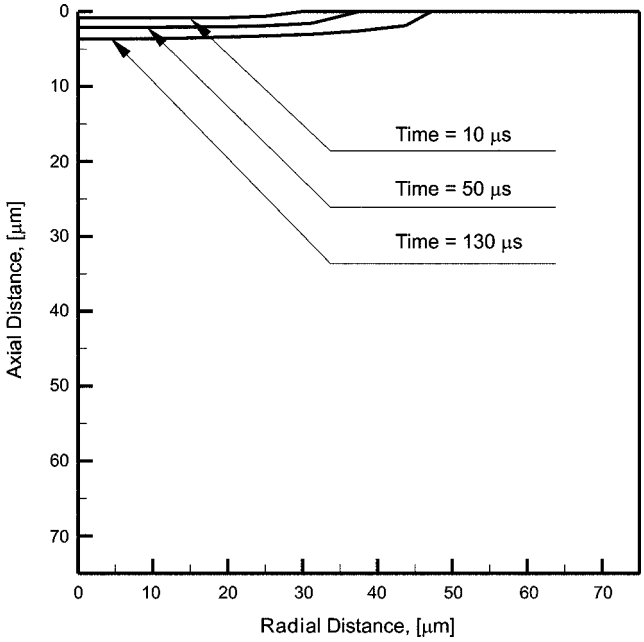

Fig. 7. Crater shape in the electro-discharge machined workpiece when 10 μs, 50 μs and 130 μs are elapsed after the onset of the on-time (current of 7 A and voltage of 51.3 V).

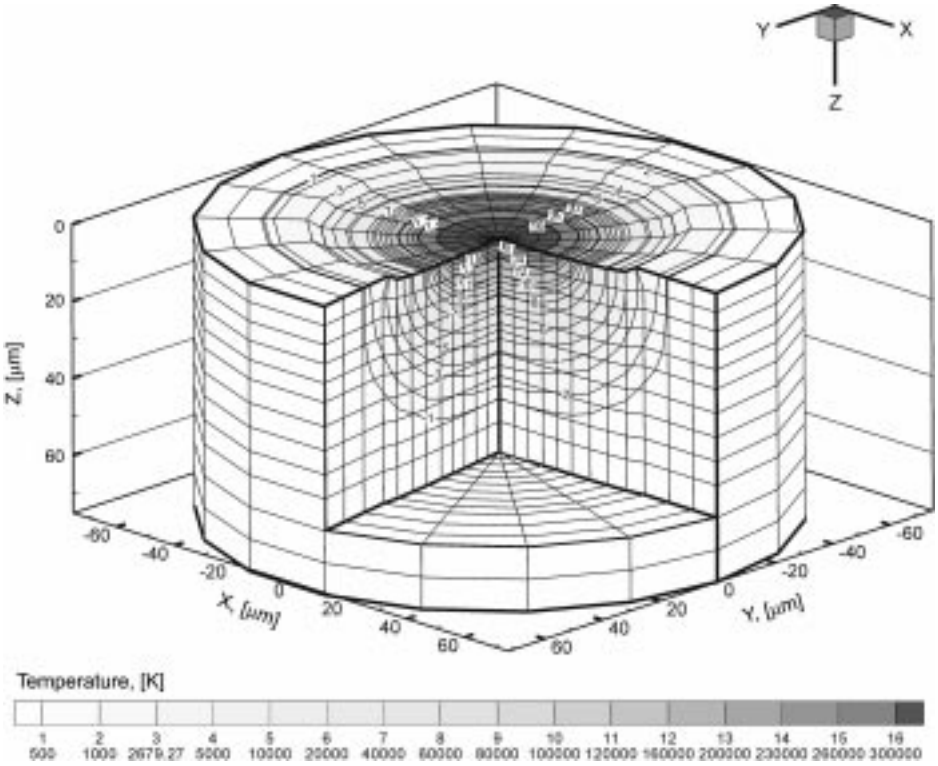

Fig. 8. Three dimensional view of the crater shape and the temperature distribution in an electro-discharge machined workpiece when 130 μs are elapsed after the onset of the on-time (current of 7 A and voltage of 51.3 V).

was assumed as in the literature [Madhu et al., 1991] in calculating the depth of the heat-affected zone for the parametric range of the process condition. The moving boundary of the crater was interpolated in every time-increment in the axial direction while the nodes at the crater's circumference were moved to the new positions of melting boundary on the surface so that the bilinear characteristic of the elements was readily maintained.

The shapes of the craters formed in the discharge time of 10, 50, and 130 μs are displayed in Fig. 7, where we can see that the crater progressively increases with time. After 10 μs the size of a crater becomes 25 μm in radius and 1 μm in depth, while after 50 μs it is increased to 35 μm in radius and 2.5 μm in depth. And finally, after 130 μs the size of the crater reaches as large as 45 μm in radius and 4 μm in depth. These results are displayed in 3D in Fig. 8. From the scanning electron micrograph of Fig. 9, it can be identified that the size and shape of the crater formed by a single spark correspond in both calculation and observation.

The electrical discharge machining process is a discrete serial appearance of sparks on the surface of a workpiece with microseconds time interval and the entire process can be identified by reviewing the results of a single spark. Therefore, based on the results

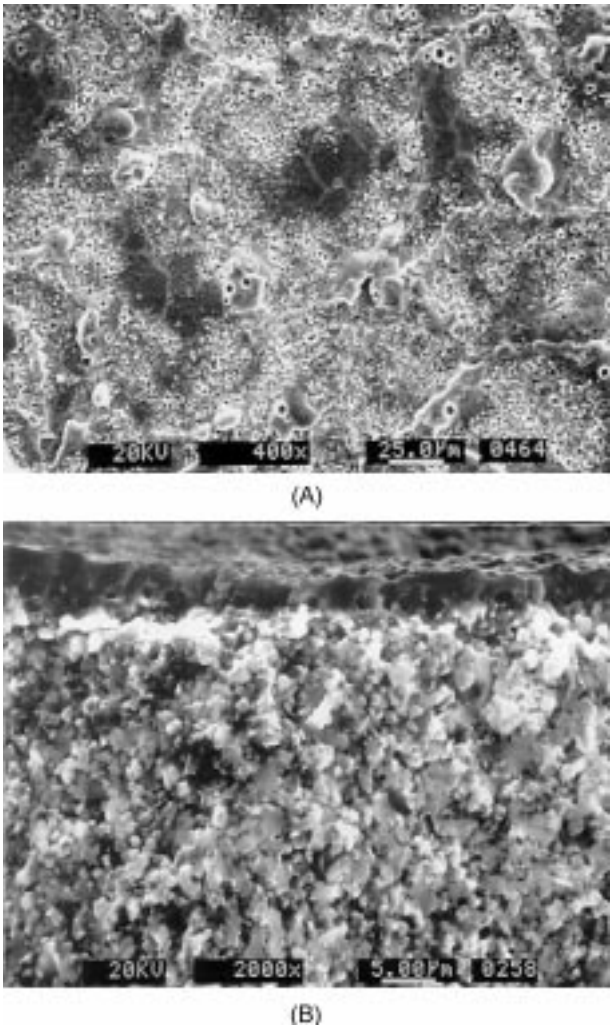

Fig. 9. Scanning electron micrographs of (A) surface and (B) cross section of an electro-discharge machined workpiece.

Table 2. Intensities of the cyclical discharges selected for the analysis

Case	Current [A]	Voltage [V]	Radius [μm]	Heat flux [cal/m^2·s]
1	4.5	33	25	1.808×10^{10}
2	7	51.3	25	2.812×10^{10}
3	11	80.7	25	4.419×10^{10}

Table 3. Time fragments and duty factors of the cyclical discharges selected for the analysis

Case	Induction time τ_w [μs]	On time τ_{on} [μs]	Off time τ_{off} [μs]	Duty factor DF
1	0	48	152	0.24
2	7	59	129	0.30
3	24	130	134	0.45

of the previous analysis the material removal rate (MRR) and the machining time of the process can be estimated for each process condition, while the relation between the surface roughness and the process condition can be identified by reviewing the size and shape of the crater.

The electric current and discharge time are the major process parameters and the electric current was converted to an equivalent discharge energy when applied. The discharge energies selected for use in the calculation are equivalent to the currents used in the previous experimental study [Wang et al., 1997; Yun et al., 1997], that is, 4.5, 7, and 11 A which correspond to the electric powers of 33, 51.3, and 80.7 V, respectively. These are equivalent to the heat fluxes of 1.808×10^{10}, 2.812×10^{10}, 4.419×10^{10} cal/m^2·s supplied through a circular area of radius 25×10^{-6} m (Table 2). The actual processing time of the electrical discharge machining consists of induction time (τ_w), on-time (τ_{on}), and off-time (τ_{off}), the values of which were selected in the previous experiments [Wang et al., 1997; Yun et al., 1997] and are shown in Table 3. In Table 3, the duty factor (DF) is the ratio of the on-time to the sum of the induction time, on-time, and off-time and means the compactness of discharge. Since the time during which the material removal occurs is the on-time, the on-time is discretized into a small time increments of 0.1 μs in the calculation.

Fig. 10 shows the three dimensional view of the craters formed for the electric currents with a duty factor of 0.24 and discharge time of 48 μm. For a current of 4.5 A the temperature increased up to 80,000 K and the size of the crater reached a diameter of 70 μm and a depth of 2 μm. With the increased current both the temperature and the size of the crater increased such that for 11 A the temperature reached 400,000 K and the size of the crater became as large as 80 μm in diameter and 3 μm in depth.

Fig. 11 describes the shape of the crater and the temperature distribution developed for each current with the duty factor of 0.45 (discharge time of 130 μs). For a current of 4.5 A the temperature reached more than 200,000 K and the size of the crater became 90 μm in diameter and 4 μm in depth. For a current of 11 A the temperature reached 800,000 K and a crater of 100 μm in diameter and 5 μm in depth was formed. Thus, since the discharge time increases with an increase of the duty factor, the size of the crater is increased

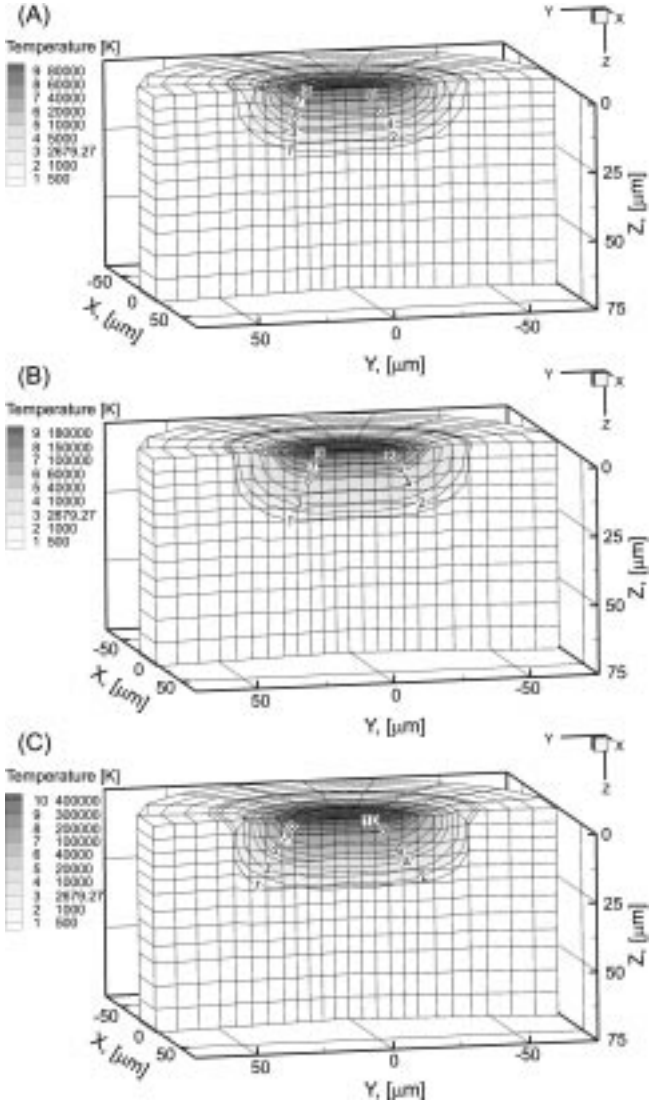

Fig. 10. The crater shapes and the temperature distributions in workpieces electro-discharge machined with currents of (A) 4.5 A, (B) 7 A and (C) 11 A (τ_{on}=48 μs, DF=0.24).

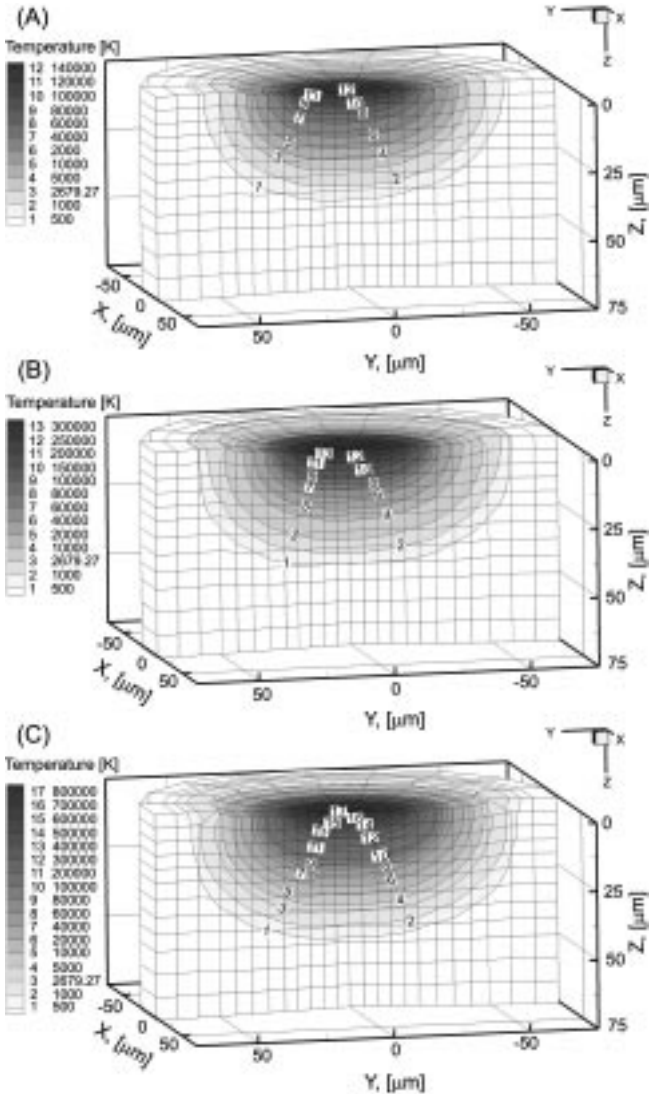

Fig. 11. The crater shapes and the temperature distributions in workpieces electro-discharge machined with currents of (A) 4.5 A, (B) 7 A and (C) 11 A (τ_{on}=130 μs, DF=0.45).

for each specified current.

Machining speed can be expressed with material removal rate (MRR), which is a function of current and duty factor. In the EDM process the head is repeatedly moving upwards and downwards to help cooling of the workpiece and removal of small chips. During the downwards motion the electrical discharge proceeds, while during the upwards motion the chips are removed. Therefore, the MRR means the machining speed measured per unit time of downward stay only, eliminating the upward stay of the head. For each duty factor the material removal rate was calculated as a function of current, as shown in Fig. 12. The material removal rate is increased with the larger electric current since the spark pits a greater amount of the workpiece material with the greater heat generated. Fig. 13 shows the material removal rate as a function of the duty factor. The increased duty factor expands the actual discharge time, which brings about a larger crater and accordingly increases the material removal rate. Thus, the material removal rate increases with the cur-

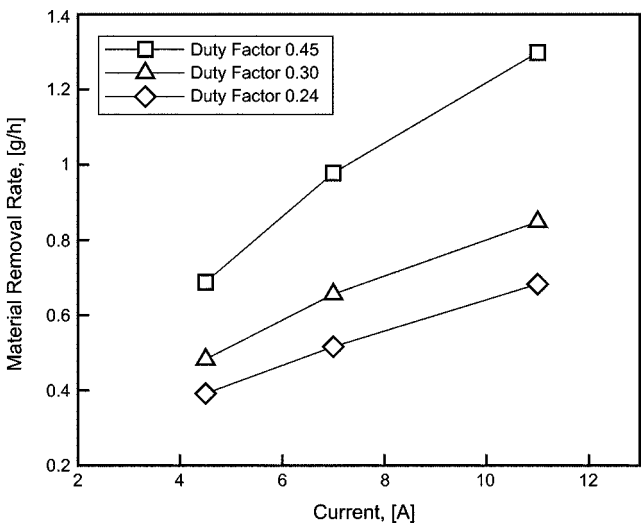

Fig. 12. Material removal rates expressed as functions of current.

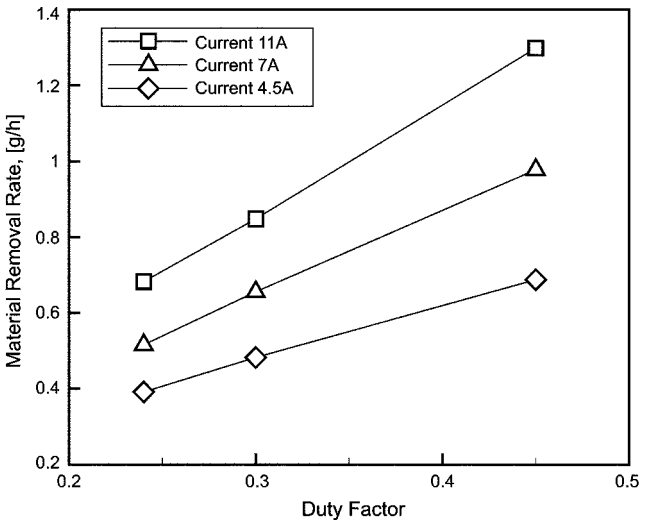

Fig. 13. Material removal rates expressed as functions of duty factor.

rent and duty factor. However, as the crater becomes larger, the roughness of the surface is increased and, as a result, the number of defects on the surface will be increased and the mechanical properties will be deteriorated. Therefore, the more the electric current and duty factor are increased, the faster the processing speed and the rougher the surface become, and vice versa. By a combination of these opposite tendencies between the processing speed and the surface roughness, the optimum processing condition can be established.

CONCLUSIONS

The electrical discharge machining process of a ceramic composite material consisting of alumina and titanium carbide has been modelled as an unsteady state mathematical model and solved using Galerkin's implicit finite element method. It has been observed that for several selected currents and powers the spark melted and sublimated the workpiece to form a crater which gradually expanded outwards. The three dimensional view of the crater as obtained by the computation was compared with the scanning electron micrograph of the cross-section of the crater formed in an experiment. For both cases, the size and shape of the crater were in good agreement. And, it was found that the increased electric current and duty factor would increase the material removal rate. However, they would also increase the size of a crater, which would lead to a roughened and defective surface, and finally to a loss of mechanical properties. Thus, through a compromise between the machining speed and the surface roughness, an optimum condition can be established.

NOMENCLATURE

C_p : specific heat [cal/kg·K]
d_c : actual thickness of removed layer [μm]
h : heat transfer coefficient between workpiece and surroundings [cal/m²·s·K]
h_r : effective radiant heat transfer coefficient [cal/m²·s·K]
k : thermal conductivity of the workpiece [cal/m·s·K]
K : stiffness matrix of the finite element equation
M : coefficient matrix in the transient term of the finite element equation
$\underline{n}$: inward normal vector to the boundary surface
$\overline{n}$: outward normal vector to the boundary surface
n_r : radial component of the outward normal vector to the boundary surface
n_z : axial component of the outward normal vector to the boundary surface
q_n : temperature gradient outward normal to the face of boundary elements
Q : heat flux of a spark [cal/s·m²], matrix of the boundary integral term
Q_n : component of the heat flux of a spark in the direction normal to the boundary surface [cal/s·m²]
Q_z : axial component of the heat flux Q [cal/s·m²]
r : radial distance [μm]
R : radius of a spark [μm]
t : time [s]
T : temperature [K]
T_0 : initial temperature [K]
T_f : temperature of dielectric fluid [K]
T_j : temperature at the j-th node of a finite element
T_m : melting point of workpiece [K]
v : bilinear shape function
z : axial distance [μm]
z_m : thickness of melted layer [μm]

Greek Letters

α : thermal diffusivity [m²/s]
Γ^e : face of a finite element
δ : depth of a crater [μm]
δ_D : thermal penetration depth [μm]
δ_r : radial derivative of the depth of a crater
ε : emissivity
η : removal efficiency
θ : polar coordinate
ρ : density [kg/m³]
σ : Boltzmann's constant
ψ_j^e : j-th shape function of a finite element
Ω^e : domain of a finite element

Superscripts

e : finite element

Subscripts

D : depth
j : node number

REFERENCES

Ahn, Y.-C., Chung, Y.-S., Wang, D.-H. and Yun, J., "Numerical Analysis of the Electro-discharge Machining Process for Alumina-Titanium Carbide Composite: I. Steady State Approach," *HWAHAK KONGHAK*, **35**, 850 (1997).

Bird, R. B., Stewart, W. E. and Lightfoot, E. N., "Transport Phenomena," Wiley, New York (1960).

Bromley, L. A., "Heat Transfer in Stable Film Boiling," *Chem. Eng. Prog.*, **46**(5), 221 (1950).

Dharmadhikari, S. W. and Sharma, C. S., "Determination of Material Removal in EDM using a Multiple Heat Source Model," IX AIMTDR Conference, IIT, Kanpur, 316 (1980).

Gadalla, A. M. and Cheng, Y.-M., "Machining of Zirconium Diboride and Its Composites," *Conf. Mach. Comp. Mater. II*, 17 (1993).

Jilani, S. T. and Pandey, P. C., "Analysis and Modelling of EDM Parameters," *Precision Eng.*, **4**(4), 215 (1982).

Jilani, S. T. and Pandey, P. C., "Analysis of Metal Removal in EDM: Effects of Metal Evaporation," *J. Eng. Prod.*, **6**, 123 (1983).

Madhu, P., Jain, V. K. and Sundararajan, T., "Analysis of EDM Process: A Finite Element Approach," *Computers Eng.*, **2**, 121 (1991).

Pandit, S. M. and Rajurkar, K. P., "A Stochastic Approach to Thermal Modeling applied to Electro-Discharge Machining," *J. Heat Transfer*, **105**, 555 (1983).

Reddy, J. N., "An Introduction to the Finite Element Method," 2nd ed., McGraw-Hill, NY (1993).

Snoeys, R. and Van Dyck, F., "Investigations of EDM Operations by Means of Thermo-Mathematical Models," *Annals of CIRP*, **20**(1), 35 (1971).

Wang, D.-H., Woo, J.-Y., Yun, J. and Ahn, Y.-C., "Electrical Discharge Machining of TiC/Al_2O_3 Ceramic Composite," *J. Korean Soc. Prec. Eng.*, **14**(9), 80 (1997).

Yun, J., Wang, D.-H., Ahn, Y.-C. and Go, C., "Electrical Discharge Machining of Alumina Ceramic Matrix Composites Containing Electro-conductive Titanium Carbide as a Second Phase," *J. Korean Ceramic Society*, **34**(10), 1092 (1997).